NJC

ROYAL SOCIETY OF CHEMISTRY

PAPER

View Article Online
View Journal

Cite this: DOI: 10.1039/d5nj05009j

Thermochromic, self-luminescent solid–solid phase change composite membranes from polyethylene glycol entanglement for thermal management, shape memory and information encryption

Xingyu Tian,[a] Yinbo Zhao *[b] and Weizhong Yuan *[a]

Phase change materials (PCMs), capable of absorbing and releasing thermal energy during phase transitions, have significant potential for thermal energy storage applications. Low molecular weight polyethylene glycol (LPEG, M_w = 8000 g mol^{-1}) stands out as an exceptional PCM owing to its environmental benignity, non-toxicity, non-corrosiveness, high storage capacity, minimal volume variation during phase transition, chemical stability, low supercooling degree, and cost-effectiveness. However, LPEG undergoes a solid–liquid phase transition, which leads to leakage issues. To address this, ultra-high molecular weight PEG (HPEG, M_w = 8 × 10^6 g mol^{-1}) was incorporated with LPEG to fabricate solid–solid phase change membranes *via* physical entanglement of internal molecular chains. These membranes exhibit excellent thermal stability and solid–solid phase transition behavior, accompanied by a high phase change enthalpy of 173.5 J g^{-1}, endowing them with superior thermal insulation performance and favorable cyclic thermal reliability. Additionally, a thermal-induced shape memory effect was achieved through the reversible crystallization–melting of HPEG molecular chains. Upon integration with thermochromic microcapsules and afterglow luminescent particles, the membranes further demonstrate thermochromic and photoluminescent properties. Consequently, the resulting solid–solid phase change composite membranes can be applied in thermal insulation for high-temperature equipment, nighttime indication, and information encryption, thereby offering a promising strategy for the development of multifunctional polymeric phase change materials.

Received 30th December 2025,
Accepted 10th March 2026

DOI: 10.1039/d5nj05009j

rsc.li/njc

Introduction

The growing global demand for energy has intensified the urgency of the energy crisis.[1–3] Thermal energy, as a widely available and easily accessible form of energy in nature, has attracted increasing attention.[4–6] Phase change materials (PCMs), which undergo phase transitions during heat absorption and release, have been extensively studied and show promising applications in thermal energy storage,[7–9] temperature regulation,[10–12] and wearable thermal management devices.[13] Based on morphological changes during phase transitions, PCMs are categorized into liquid–liquid, liquid–gas, solid–liquid, and solid–solid types.[14] Among these, solid–liquid PCMs are widely utilized due to their advantages of readily available raw materials, high phase change enthalpy, and flexibly tunable phase change temperatures.[15] Polyethylene glycol (PEG), as an organic polymeric solid–liquid PCM, has garnered significant interest owing to its ease of processing, excellent durability, adjustable molecular weight, and high heat storage capacity.[8,16,17]

However, solid–liquid PCMs undergo a solid-to-liquid transition during phase change, leading to risks of leakage and phase separation.[18] Additionally, their poor shape stability resulting from this transformation severely limits practical applications.[19] To address these issues, various encapsulation strategies have been developed for leak-prone PCMs. Yang *et al.* designed a porous cellulose nanofiber (CNF) scaffold to encapsulate PEG, effectively mitigating leakage during phase transitions.[20] He *et al.* developed MXene/silver nanowire composite sponges and encapsulated PEG *via* vacuum impregnation.[21] Bai *et al.* prepared polyvinyl alcohol (PVA)/sodium alginate (SA) aerogels with a multilayered network structure using wet spinning and freeze–thaw cycling, followed by loading PEG and

[a] School of Materials Science and Engineering, Key Laboratory of Advanced Civil Materials of Ministry of Education, Tongji University, Shanghai, 201804, People's Republic of China. E-mail: yuanwz@tongji.edu.cn
[b] School of Aerospace Engineering and Applied Mechanics, Tongji University, Shanghai, 200092, People's Republic of China. E-mail: yinbozhao@tongji.edu.cn

nano-ZnO into the aerogel pores *via* vacuum impregnation.[22] Yan *et al.* fabricated a series of ethylene glycol/polyethylene glycol (EG/PEG) composites with tuneable mass fractions *via* a physical adsorption strategy, using EG as the matrix material.[23] By modulating the EG-to-PEG mass ratio, they tailored the thermal conductivity of the resultant composites and systematically investigated the impacts of matrix mass fraction and light intensity on their energy conversion characteristics. The as-prepared phase-change composites exhibited superior thermal conductivity, favourable phase-change behaviour, and efficient photoelectric/electrothermal conversion performance, thus demonstrating great potential for applications in multi-physics energy conversion and high-grade energy utilization. Nonetheless, these approaches require encapsulating PEG within shell materials, which reduces the PEG content and consequently diminishes the phase change enthalpy.[18] Moreover, PEG still exhibits liquid-phase behavior during temperature-induced phase change, retaining leakage potential.[24] These approaches necessitate the incorporation of non-functional materials,[25] reducing the proportion of PCM and diminishing the phase change enthalpy.

Solid–solid PCMs represent a promising alternative to solid–liquid PCMs.[14] They maintain a solid state before and after phase transition without undergoing shape changes, ensuring dimensional stability while eliminating leakage risks. The conventional approach to preparing solid–solid PCMs involves chemically crosslinking PU and low molecular weight PEG (LPEG).[26,27] PU uses cyanate as a catalyst to capture hydrogen bonds on LPEG for crosslinking. While this method enables solid-state phase change, the preparation process is complex with low success rates. Moreover, the use of cyanate-containing reagents poses significant toxicity risks and is environmentally unfriendly. Furthermore, chemical cross-linking restricts PEG molecular chain mobility, resulting in low crystallinity and reduced phase change enthalpy. The cross-linked structure also hinders recycling, causing environmental pressure. Therefore, it is essential to develop a facile fabrication method to obtain solid–solid PCMs with shape-stability, high phase change enthalpy, environmental friendliness, and reusable performance.

Recently, significant attention has been devoted to ultra-high molecular weight polyethylene glycol (HPEG) in PCMs.[28] Owing to its long molecular chains and random physical entanglement, HPEG exhibits a relatively high phase transition temperature without undergoing a distinct solid–liquid phase change.[27,29] At elevated temperatures, it only softens – an attribute that endows it with superior thermal stability compared to LPEG. With inherent solid–solid phase transition characteristics, HPEG is regarded as an ideal candidate for solid–solid phase change applications. However, its relatively low phase transition enthalpy and poor processability have hindered its further practical utilization. By contrast, LPEG features higher phase transition enthalpy values; its shorter molecular chains also result in fewer random physical entanglement sites,[30] which differs from HPEG's structural behavior.

When HPEG and LPEG are blended, the long molecular chains of HPEG entangle with those of LPEG, forming a physically crosslinked structure.[28,31] This structure extends the molecular relaxation time, maintains the composite in a solid state, and thereby prevents leakage.[32,33] Meanwhile, the physically crosslinked network preserves the high crystallinity of LPEG, with HPEG acting as a supportive matrix to retain the phase change enthalpy.[34] Thus, HPEG–LPEG can achieve solid–solid phase transitions while maintaining high thermal enthalpy. LPEG acting as the phase change component tends to reduce the mechanical properties of the composite PCMs. It is therefore necessary to optimize the mass ratio of HPEG to LPEG to balance high thermal enthalpy and desirable mechanical performance.[35] Additionally, the multi-functionalization of PCMs represents a key trend in their development. Incorporating functional particles (thermochromic particles and photoluminescent particles) enables PCMs to acquire versatile functionalities,[36] which in turn expands their application potential in thermal management scenarios.[10,37]

Herein, the multifunctional solid–solid phase change membranes were designed and fabricated, leveraging the physical entanglement of HPEG chains with LPEG at different mass ratios (Fig. 1). In the HPEG–LPEG system, HPEG serves as a supporting skeleton that imparts solid-state phase change behavior and as a crystallizable component, while LPEG functions exclusively as the phase change component. The intermolecular entanglement between HPEG and LPEG enables the membrane to achieve both solid-state phase transition and thermal insulation performance. Notably, the ultra-long molecular chains of HPEG endow the membrane with a high phase change enthalpy (170 J g^{-1}), excellent thermal stability (maintaining structural integrity at 90 °C), and superior insulation properties. It also exhibits outstanding shape retention capability and infrared shielding performance. Additionally, the reversible crystallization–melting behavior of HPEG molecular chains endows the phase change membrane with thermally induced shape memory functionality. When integrated with

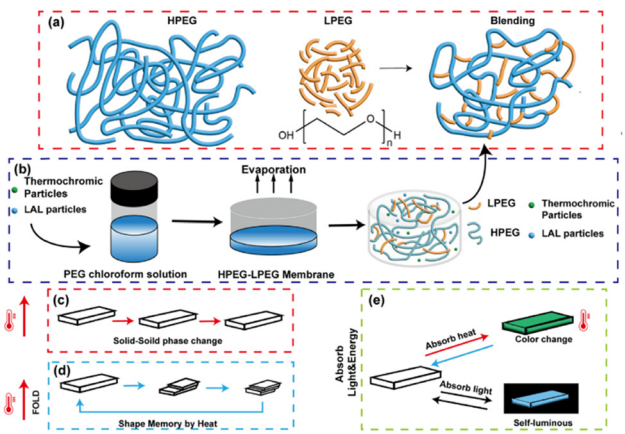

Fig. 1 (a) Schematic molecular chains of HPEG–LPEFG solid–solid phase change membranes. (b) Schematic preparation of HPEG–LPEG solid–solid phase change membranes. (c) Solid–solid phase change process of HPEG–LPEG membranes. (d) Heat-induced shape memory of HPEG–LPEG solid–solid phase change membranes. (e) Thermochromic and fluorescent of HPEG–LPEG solid–solid phase change membranes.

thermochromic microcapsules, the membrane forms a composite system with potential applications in information encryption. Simultaneously, the incorporation of photoluminescent particles (LAL) enables the membrane to absorb sunlight during the day and emit light continuously at night. Specifically, the LAL-doped HPEG–LPEG solid–solid phase change membranes can emit light for an extended period (2 h) after only a short-duration of light absorption (30 min). This design strategy paves a new way for developing PCMs with additional functionalities beyond traditional thermal energy storage, presenting promising application prospects in road signage, emergency lighting, smart buildings, and smart highways.

Experimental section

Materials

HPEG (M_w = 8 × 10^6 g mol^{-1}) and LPEG (M_w = 8000 g mol^{-1}) were purchased from Aladdin Reagent Co., Ltd, Shanghai. Chloromethane was purchased from Sinopharm Chemical Reagent Co., Ltd. Photoluminescent materials (LAL, the main ingredients are strontium aluminum sulfate doped with europium and dysprosium) were purchased from Shandong Yousu Chemical Technology Co., Ltd. Thermochromic microcapsules (polyoxymethylene melamine, Laury alcohol, cetyl alcohol mixture) were purchased from Shenzhen Oriental Thermochromic Technology Co., Ltd. All the chemicals were of analytical grade and used as received.

Preparation of HPEG–LPEG solid–solid phase change membranes

The HPEG–LPEG solid–solid phase change membranes were prepared *via* physical blending: HPEG and LPEG were mixed in 10 mL chloroform at different mass ratios to form 9 samples with different ratios of HPEG to LPEG. The detailed ratios are listed in Table 1. Each mixture was stirred for 30 h to obtain a homogeneous solution, which was subsequently poured into molds and placed in a fume hood for 8 h to facilitate solvent evaporation. The homogeneous solution was poured into a mold to a depth of 5 mm, filling the mold completely. Then maintain the oven temperature at 25 °C. After 30 h, a HPEG–LPEG solid–solid phase change membrane of uniform thickness will be obtained.

Table 1 Phase change membranes with different masses of HPLG and LPEG

Sample	Mass of HPEG (g)	Mass of LPEG (g)
A1	0.04	0.16
A2	0.08	0.12
A3	0.12	0.08
B1	0.06	0.24
B2	0.12	0.18
B3	0.24	0.06
C1	0.10	0.40
C2	0.20	0.30
C3	0.40	0.10

Preparation of thermochromic solid–solid phase change membranes

After stirring sample B2 for 24 h, 0.2 g of thermochromic microcapsules were added. After stirring for an additional 6 h to form a homogeneous solution, the mixture was allowed to stand for 1 h. Finally, it was poured into a mold and placed in a fume hood for evaporation. After 8 h of evaporation, thermochromic solid–solid phase change membranes were prepared.

Preparation of self-luminescent solid–solid phase change membranes

After blending sample B2 for 24 h, 0.2 g (2%) of LAL nanoparticles were added. After stirring for an additional 8 h to form a homogeneous solution, the mixture was allowed to stand for 1 h. Finally, it was poured into a mold and placed in a fume hood for evaporation. Following 8 h of evaporation, LAL solid–solid phase change membranes were prepared.

Characterization

Scanning electron microscopy (SEM). The morphology characteristics of samples were examined by emission scanning electron microscopy (SEM, FEI-QUANTA-FEG250).

X-ray diffraction (XRD) and polarized optical microscopy (POM). The crystallization characteristics were determined using polarized light microscopy and X-ray powder diffraction patterns (XRD) (D8, Bruker) with a scanning angle from 10° to 60° at a speed of 5° min^{-1}. An XS-402 polarized optical microscope (Shanghai Microimage Technology, China) was utilized to observe the crystalline morphological images of the samples. In short, the samples were placed on a glass plate mounted on a heating stage, and the temperature was increased from room temperature to 100 °C at a heating rate of 10 °C min^{-1}.

Differential scanning calorimetry (DSC). The heating and cooling enthalpies of the samples were studied by differential scanning calorimetry (DSC) with heating and cooling from 10 to 90 °C in a nitrogen atmosphere at a rate of 10 °C min^{-1}.

Thermal gravimetric analysis (TGA). Thermal properties of the samples were measured in the 30–800 °C range using a thermogravimetric analyzer (TG, Q600, TA Instruments) at a heating rate of 20 $°C^{-1}$.

Thermal conductivity. We measured the thermal conductivity of the samples using a thermal conductivity tester (Hot Disk TPS2500S, Sweden). The side length of the sample is 20 mm, and its thickness is 3 mm. The measurement is conducted at a test temperature of 25 °C and in the thickness direction.

Fourier transform infrared spectrometry (FT-IR). The samples were characterized *via* Fourier transform infrared spectra (FT-IR) (U-4100, Hitachi).

Fluorescence properties. The photoluminescence emission spectra, photoluminescence excitation spectra and the afterglow decay curve of the samples were measured with FLS1000 fluorescence spectrometers (Edinburgh Instruments, UK) equipped with a 450 W Xenon lamp as the excitation source.

Temperature–time curves. The time–temperature curves were measured and recorded using thermocouples and a data

acquisition system (Fluke 2638A), and an infrared thermal imaging camera was used to observe the temperature change of solid–solid phase change membranes.

Mechanical properties. The stress–strain curves were obtained using a tensile testing machine (TSE504C, Shenzhen Wance Testing Machine Co., Ltd) at a tensile speed of 10 mm min^{-1}. The film lengths were 5 cm, at a tensile speed of 10 mm min^{-1}.

Rheological properties. The rheological properties of the solid–solid phase change membranes were evaluated using an Anton Paar MCR302 rheometer, equipped with a parallel-plate geometry (diameter = 20 mm) and a fixed gap of 1 mm between the plates, with the initial temperature set at 25 °C. The experimental protocol was designed as follows: (1) strain sweep test: the storage modulus (G') and loss modulus (G'') of the membranes were assessed by gradually increasing the strain amplitude from 1% to 10% at a constant oscillation frequency of 1 Hz. (2) Frequency sweep: measurement of G' and G'' at a fixed temperature of 25 °C and a strain of 1%, varying the scanning angular frequency from 0.01 rad s^{-1} to 100 rad s^{-1}. (3) Temperature sweep test: The temperature was increased from 25 °C to 60 °C at a heating rate of 1.8 °C min^{-1}.

Results and discussion

Preparation of HPEG–LPEG solid–solid phase change membranes

The preparation process of HPEG–LPEG solid–solid phase change membranes involves blending, stirring, and solvent evaporation. During physical blending, LPEG molecular chains entangle randomly with HPEG without chemical reactions, and this blending process enhances the overall crystallinity compared to pure HPEG.[38] After blending, the solvent was poured into a mould and dried to form membranes. The prepared HPEG–LPEG solid–solid phase change membranes undergo stretching, during which the random physical entanglement of HPEG–LPEG molecular chains forms an interwoven network structure. The entanglement points act like countless microscopic "molecular anchors", connecting the originally independent molecular chains into a unified network.[39,40] When subjected to tensile stress, the material dissipates stress through segment slippage and disentanglement, preventing fracture caused by stress concentration.[41] This method significantly enhances the material's resistance to tensile deformation. Among all samples, sample B exhibited superior film-forming and mechanical properties, with sample B2 (relative to B1 and B3) showing optimal processability and moderate thickness. Additionally, increasing HPEG content enhanced film rigidity and mechanical properties as shown in Fig. S5, and the fracture length of phase change films increased with HPEG addition compared to films without HPEG, so we selected sample B for testing.

Thermal and mechanical properties of solid–solid phase change membranes

Fig. 2 shows the POM images of sample B2 at various temperatures. At room temperature, the sample exhibits a distinct

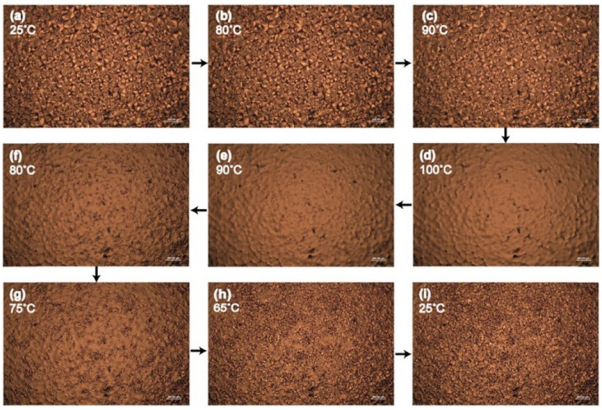

Fig. 2 POM images of sample B2 during heating processes at (a) 25 °C, (b) 80 °C, (c) 90 °C, and (d) 100 °C, and cooling processes at (e) 90 °C, (f) 80 °C, (g) 75 °C, (h) 65 °C, and (i) 25 °C.

crystalline structure, which is attributed to the random entanglement between HPEG and LPEG chains. Within a specific temperature range (below 80 °C), this crystalline structure remains intact. However, when the temperature exceeds 80 °C, the crystalline domains gradually diminish with increasing temperature and disappear entirely at 100 °C. Upon cooling, the crystalline structure progressively regenerates as the temperature decreases, fully recovering by 65 °C. This reversible temperature-driven crystallization behaviour of PEG underpins its phase change enthalpy: as the temperature rises, the crystalline structure gradually melts while absorbing heat, with maximum heat absorption occurring upon complete melting. Conversely, as the temperature decreases, the crystalline structure reforms, accompanied by heat release. The entire process realizes thermal energy storage and release through the dissolution and regeneration of PEG crystals, which also accounts for the heat-induced shape memory effect. Furthermore, due to the random entanglement of HPEG and LPEG molecular chains, HPEG plays dual roles as both a supporting matrix and a phase change component. Within a certain temperature range, its molecular chains cannot disentangle, ensuring the material retains solid-state characteristics even after reaching the phase transition temperature – thus achieving a solid–solid phase transition.[42] The POM images of samples A2 and C2 are provided in Fig. S1 and S2. Similar to sample B2, samples A2 and C2 also exhibited the disappearance of crystalline structures upon heating, which shows the heat storage mechanism arising from the crystalline structure disruption during the phase transition of PEG. However, a distinctive phenomenon was observed for sample A2: its double-cross structure vanished irreversibly after heating. This unique behaviour can be attributed to the low content (20%) of HPEG in sample A2, with LPEG serving as the dominant component. Specifically, the LPEG chains are relatively short and feature a high proportion of terminal hydroxyl groups. The strong polarity of these hydroxyl groups disrupts the regular packing of the main chains *via* hydrogen bonding interactions and steric hindrance effects. Meanwhile, the short molecular chains of LPEG fail to form

sufficiently long ordered segments required for stable crystal growth, leading to inferior segment stacking integrity and thus reduced crystallinity.[43] As a result, the crystalline structure of sample A2 is prone to disruption upon heating and difficult to regenerate during subsequent cooling.

Fig. 3 illustrates the thermal properties of the solid–solid phase change membranes. The phase transition enthalpy determines their thermal energy storage capacity.[44] DSC was employed to characterize the phase transition behaviour of samples A, B, and C, with representative results shown in Fig. 3. The detailed enthalpy values and phase transition temperatures are listed in Table 2. As depicted in Fig. 3a, the thermodynamic enthalpy of the solid–solid phase change membranes is dependent on the LPEG content. Pure HPEG exhibits stable melting enthalpy (ΔH_m) and crystallization enthalpy (ΔH_c) of 125.92 J g^{-1} and 121.07 J g^{-1}, respectively (Fig. S3). The reduced crystallinity of HPEG – arising from its longer molecular chains – contributes to its relatively low enthalpy. In contrast, LPEG features weaker molecular entanglement and shorter chains, resulting in higher thermal enthalpy.[43] This explains the results in Table 2. Increasing HPEG content leads to a decrease in the ΔH_m and ΔH_c of samples A, B, and C. Fig. 3a further confirms that the HPEG–LPEG blends achieve solid–solid phase transition. Compared to fully entangled HPEG, LPEG with weaker entanglement interactions exhibits significantly higher crystallinity and corresponding melting enthalpy. HPEG molecular chains exhibit more random entanglement than LPEG. During heating, these entangled chains resist

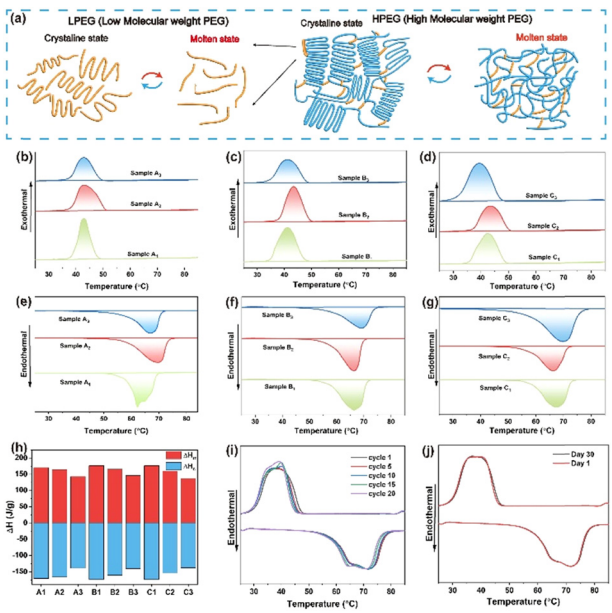

Fig. 3 (a) Schematic illustration of the solid phase change mechanism of solid–solid phase change membranes. (b)–(g) Heating and cooling DSC curves of solid–solid phase change membranes with different concentrations. (h) Phase change enthalpy of solid–solid phase change membranes with different concentrations. (i) Thermal cycling stability of solid–solid phase change membranes after 5, 10, 15, and 20 cycles. (j) Long-term thermal stability of solid–solid phase change membranes after 30 days of storage.

Table 2 Thermal properties of solid–solid phase change membranes

Sample[a]	ΔH_m (J g^{-1})	ΔH_c (J g^{-1})	T_m (°C)	T_c (°C)	Supercooling (°C)
A1	170.7	170.5	59.8	46.3	13.5
A2	164.7	165.8	62.3	44.6	17.7
A3	143.1	138.2	68.9	44.8	24.1
B1	176.5	173.3	66.2	46.2	20.0
B2	165.9	160.4	67.3	44.6	22.7
B3	146.1	140.1	69.8	45.8	24.0
C1	176.7	173.5	65.2	45.2	20.0
C2	160.2	153.8	67.8	44.8	23.0
C3	137.4	137.2	71.6	42.1	29.5
C3-5	132.4	131.1	71.3	41.9	29.6
C3-10	131.5	130.1	71.0	41.5	29.5
C3-15	130.3	129.8	70.6	41.3	29.3
C3-20	129.8	128.7	70.1	41.0	29.1

[a] The samples of A1-C3 in Table 2 are similar to those in Table 1. C3-5, C3-10, C3-15 and C3-20 denote the cycling times of C3 for 5, 10, 15 and 20 times.

disentanglement, leading to a higher melting temperature than LPEG.[44,45] This further accounts for the increasing melting temperature with rising HPEG content, as shown in Table 2. However, higher HPEG content also enhances random molecular entanglement within the solid–solid phase change material, elevating the system's crystallization energy barrier. This requires lower temperatures to initiate crystallization, which explains the following trends across samples A, B, and C: as HPEG content increased, melting temperatures rose from 58.9 °C to 68.9 °C, 66.2 °C to 69.8 °C, and 67.8 °C to 71.6 °C, respectively, while crystallization temperatures decreased from 46.3 °C to 44.8 °C, 46.2 °C to 45.8 °C, and 44.8 °C to 42.1 °C, respectively. According to the definition of undercooling, a decrease in crystallization temperature (T_c) coupled with an increase in melting temperature (T_m) results in a gradual increase in undercooling. This trend is consistent with the enhanced inhibition of the crystallization process induced by molecular chain entanglement constraints, with the undercooling values increasing from 13.5 °C to 24.1 °C, 20.0 °C to 24 °C, and 20 °C to 29.5 °C, respectively. Fig. 3h presents the melting and crystallization enthalpy values of the solid–solid PCMs. DSC curves reveal that as HPEG content decreased, the melting enthalpies of samples A, B, and C increased from 143.1 J g^{-1} to 170.7 J g^{-1}, 146.1 J g^{-1} to 176.5 J g^{-1}, and 137.4 J g^{-1} to 176.7 J g^{-1}, respectively. Concurrently, their crystallization enthalpies increased from 138.2 J g^{-1} to 170.5 J g^{-1}, 140.1 J g^{-1} to 173.3 J g^{-1}, and 137.2 J g^{-1} to 173.5 J g^{-1}, respectively. These results align with the variation in HPEG–LPEG content, demonstrating the potential of these blends for developing high phase transition enthalpy materials. In addition, thermal cycling stability is critical for real applications, and the phase transition performance of the solid–solid phase change membranes remains stable after 20 cycles (Fig. 3i), demonstrating excellent cyclic durability. The detailed melting crystallization enthalpies and temperatures at different cycle numbers (5, 10, 15, and 20 cycles) are summarized in Table 2, confirming that both enthalpies remain nearly unchanged throughout cycling. Furthermore, after 30 days of storage, DSC curves remain unchanged, confirming long-term phase stability and reliability (Fig. 3j).

TGA was conducted to evaluate the thermal stability of the solid–solid phase change membranes, as shown in Fig. S4. The TGA curves show minimal initial weight loss below 320 °C; samples A2, B2, and C2 exhibited similar thermal degradation behaviour, with major weight loss occurring at ~350 °C – corresponding to the decomposition of PEG.[43] In the range of 300–350 °C, the samples maintained relatively stable weight, indicating good thermal stability within this temperature window. Above 350 °C, significant weight loss was observed, attributed to the thermal decomposition of the HPEG–LPEG structure. Notably, sample C2 retained a higher residual mass at elevated temperatures compared to sample A2, suggesting that HPEG enhances the thermal stability of the solid–solid phase change membranes. This improvement can be ascribed to the rigid random entanglement of HPEG molecular chains, which may offer advantages for high-temperature applications.

Fig. S5 shows the mechanical properties of sample B and LPEG membranes. It is evident that LPEG membranes exhibit inferior mechanical performance, with a tensile strength of merely 2 MPa and an elongation at break of 100%. In contrast, the incorporation of HPEG enhances the tensile properties of the HPEG–LPEG membranes, which attain a tensile strength of 4 MPa and an elongation at break approximately four times that of LPEG membranes. This mechanical reinforcement originates from the physical random entanglement of molecular chains.[46] Under tensile loading, these randomly distributed physical entanglements act as topological constraints that effectively impede the rapid propagation of microcracks and delay the occurrence of catastrophic fracture. With the continuous application of tensile stress, these entangled chain segments undergo gradual disentanglement and orientation along the stretching direction, which accounts for the substantially elevated elongation at break of the HPEG–LPEG composite films.

Thermal stability of solid–solid phase change membranes

Fig. 4 illustrates the thermal stability of samples A, B, and C, focusing on the shape stability and leakage behaviour of PEG with different molecular weights. Solid–solid phase change materials composed of HPEG, LPEG, and the resultant solid–solid PCMs were heated from room temperature (25 °C) to 90 °C, with morphological changes monitored throughout the process. Fig. 4(I, II) and (III, IV) depict the behaviour of LPEG and HPEG at room temperature and 90 °C, respectively. As temperature increases, the molecular chain entanglement of LPEG is disrupted, causing it to transition from a solid to a liquid state – indicating a significant leakage risk. In contrast, HPEG maintains tightly randomized molecular chain entanglement that resists disruption with rising temperature, thus preserving its solid-state phase transition characteristics. Fig. 4(V–X) show the morphological behaviour of samples A, B, and C at different temperatures. All solid–solid phase change membranes exhibit solid-state phase transition characteristics, with overall shape stability improving as HPEG content increases. Fig. 4(V) reveals that at lower HPEG concentrations, the samples tend to melt as temperature rises; however, the disordered entanglement between HPEG and LPEG molecules restricts chain mobility, thereby retaining solid-state properties. Fig. 4(X) demonstrates that at higher HPEG proportions (HPEG–LPEG concentration of 50 mg mL^{-1}), the samples exhibit markedly enhanced shape stability under temperature variation, with distinct solid-state phase transition features. When the HPEG–LPEG concentration is 30 mg mL^{-1} (Fig. 4(IX)), sample B shows superior shape stability during heating compared to sample A. Increasing HPEG proportion leads to enhanced random entanglement of molecular chains. As the temperature rises, this entanglement resists molecular chain movement, enabling the material to remain in a solid state.[28] The incorporation of HPEG thus significantly improves shape stability, making solid–solid phase change membranes a promising candidate for solid-phase change applications and thermal management systems.

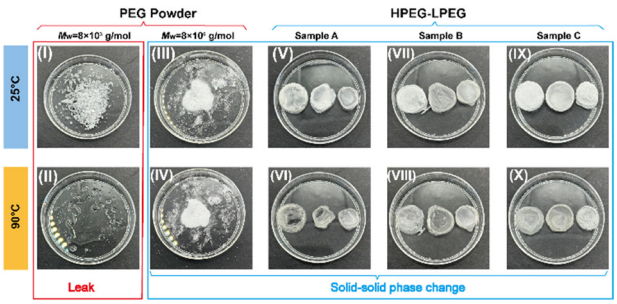

Fig. 4 Comparison of the shape stability and leakage behavior of LPEG and HPEG and their composites at different temperatures. (I) and (II) Pure LPEG at 25 °C and 90 °C, (III) and (IV) pure HPEG at 25 °C and 90 °C, (V) and (VI) sample A at 25 °C and 90 °C, (VII) and (VIII) sample B at 25 °C and 90 °C, and (IX) and (X) sample C at 25 °C and 90 °C.

Thermal insulation properties of solid–solid phase change membranes

Fig. 5a illustrates the thermal insulation mechanism of the solid–solid phase change membranes, which stems from their phase change-induced heat storage and release behaviour. Due to the stable physical entanglement, high degree of random molecular entanglement, and restricted chain mobility in the HPEG–LPEG system, heat transfer *via* molecular vibrations is impeded when the material is heated.[47] Meanwhile, the disruption of crystalline structures within the solid–solid phase change membranes enables thermal energy storage, while the material's surface temperature remains constant creating a temperature difference (ΔT) between the two sides of the membrane.[48] As shown in Fig. 5b, samples A2, B2, and C2 (each with a thickness of 0.5 cm) were placed in direct contact with a hotplate (the heat source). When the hotplate temperature was maintained at 60 °C, the ΔT values of samples A2, B2, and C2 relative to the heat source were 9 °C, 12 °C, and 15 °C, respectively. Increasing HPEG content enhanced the disordered physical entanglement of molecular chains, further hindering heat transfer *via* molecular vibrations during heating and thereby improving thermal insulation capacity. This explains the sequential increase in ΔT between samples A2/B2/C2 and the hotplate. Rheological testing also confirmed this. Fig. 5c

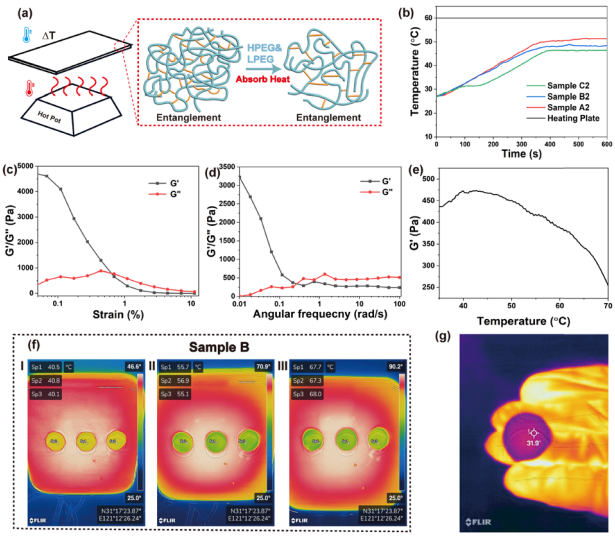

Fig. 5 (a) Schematic illustration of the thermal insulation mechanism of solid–solid phase change membranes. (b) Time–temperature curve of samples A2, B2, and C2 at 60 °C. (c) Variation of storage modulus and loss modulus with strain at 25 °C. (d) Variation of storage modulus and loss modulus with frequency at 25 °C. (e) Rheological storage modulus of solid–solid phase change membranes at different temperatures. (f) Thermal insulation properties of sample B at 50 °C, 70 °C and 90 °C. (g) Infrared images of the sample B2 placed on a human palm.

demonstrates the variation of G' and G'' with strain for solid–solid phase change membranes at 25 °C. At low strain levels, G' was greater than G'', indicating a solid state. However, at approximately 0.07% strain, a crossover point was reached where G' became less than G', marking the destruction of the solid state. This is primarily because, in the low strain region (<1%), the dense physical entanglement network formed by HPEG's ultra-long molecular chains remains intact. Elastic contributions dominate material behaviour, resulting in a significantly higher storage modulus G' than loss modulus G'', giving the material a solid-like state. When strain exceeds the critical threshold of 1%, the entanglement network dissociates due to large deformation, causing a sharp decline in elastic constraint capability and a rapid decrease in G'. Simultaneously, viscous flow induced by molecular chain slip intensifies, leading G'' to surpass G'. The material then transitions to a viscous-dominated flow state. Fig. 5d displays the frequency-dependent behavior of G' and G'' for the solid–solid phase change membranes at 25 °C. When the angular frequency is less than 1 rad s^{-1}, the storage modulus G' is significantly higher than the loss modulus G'', and G' decreases rapidly as angular frequency increases. When angular frequency exceeds 1 rad s^{-1}, G' continues to decrease while G'' gradually increases, ultimately surpassing G' and stabilizing. This change mainly originates from the frequency response characteristics of the HPEG–LPEG entanglement network: at low frequencies, molecular chains have sufficient time to relax, and the dense entanglement network of HPEG maintains elastic dominance, resulting in G' being significantly higher than G''. As frequency increases, the relaxation rate of molecular chains cannot match the external vibration frequency, weakening the elastic constraints of the entanglement network and causing G'' to decrease. Concurrently, at high frequencies, molecular chain slip intensifies, amplifying the viscous flow contribution, causing G'' to rise and surpass G'. This reflects the viscoelastic transition of the HEPG–LPEG system under dynamic loading-shifting from "low-frequency elasticity dominance" to "high-frequency viscosity dominance". At its core, this phenomenon stems from the frequency-dependent synergistic interaction between the HPEG–LPEG entanglement network and molecular chain motion. Fig. 5e illustrates the temperature-dependent curves of G' for solid–solid phase change membranes. At the initial temperature of 25 °C, G' is approximately 440 Pa, decreasing only slowly as the temperature rises to 45 °C. Notably, when the temperature exceeds 45 °C, the solid–solid phase change membranes exhibited significantly decreased G' values, dropping to approximately 250 Pa at 70 °C. The critical transition point of this change occurs at 45 °C, stemming from the synergistic regulation of temperature on the system's entangled network and phase-transition behaviour: Within the 25–45 °C range, rising temperature merely enhances thermal motion in some molecular chains. The dense entangled network of HPEG does not undergo significant dissociation, with only a few weak entanglement points breaking. Consequently, G' decreases gradually. Upon reaching 45 °C, thermal motion energy surpasses the critical dissociation threshold of the HPEG entanglement network, while LPEG begins extensive melting. LPEG melting not only increases molecular chain slip space but also further weakens HPEG chain interactions, causing rapid disintegration of the entanglement network and a sharp decline in elastic constraint capacity. Thus, the G' decline rate significantly accelerates after 45 °C. The change at 45 °C represents the "thermal softening critical temperature" of this system: before this temperature, the HPEG entanglement network dominates the material's elasticity (solid-like state); after this temperature, network dissociation and LPEG melting jointly drive the material's transition toward a viscous-dominated state. This provides key rheological evidence for designing its thermal response range and shape stability as a phase-change material. What's more, the thermal conductivity of the solid–solid phase change membranes is 0.58 W $(m\ K)^{-1}$. The intrinsic thermal conductivity of LPEG is only 0.25 W $(m\ K)^{-1}$. In contrast, HPEG as the component, forms a continuous physical entanglement network through its ultra-long molecular chains. However, its overall thermal conductivity remains relatively low, which explains its thermal insulation properties. Fig. 5f presents the surface temperatures of samples A, B, and C measured after placing them on heating stages set to 50 °C, 70 °C, and 90 °C. As the heating stage temperature increased, the surface temperatures of all samples rose, and their ΔT relative to the stage increased from 6 °C (at 50 °C) to 15 °C (at 70 °C) and further to 23 °C (at 90 °C) – with the maximum ΔT of 23 °C observed at 90 °C. At each identical heating temperature, the surface temperatures of samples A, B, and C were relatively close: 40.8 °C, 40.5 °C, and 40.1 °C (at 50 °C); 56.9 °C, 55.1 °C, and 55.7 °C (at 70 °C); and 67.3 °C, 67.7 °C, and 68.0 °C

(at 90 °C). This similarity is attributed to the relatively comparable HPEG contents across the three sample systems. Additionally, the vibrational frequencies of the C–C and C–H bonds in PEG are incompatible with infrared (IR) energy, preventing efficient absorption of IR radiation.[49] Most IR radiation either transmits through the material or is reflected, rather than being absorbed and converted into heat. This reduces heat accumulation caused by IR radiation, endowing the solid–solid phase change membranes with IR shielding properties (Fig. 5g). Collectively, these thermal insulation and IR shielding capabilities highlight the potential of the solid–solid phase change membranes for applications in IR shielding and thermal insulation materials.

Shape memory and thermochromic properties of solid–solid phase change membranes

Fig. 6 demonstrates the thermally induced shape memory performance of the solid–solid phase change membranes in more complex geometries. Fig. 6a illustrates the morphological transformation of the phase change membranes before and after HPEG incorporation. Prior to HPEG addition, the pure LPEG-based phase change membrane exhibited inherent brittleness-attributed to the weak molecular entanglement and short chain length of LPEG and fractured when folded. Fig. 6b shows that after introducing HPEG, its longer molecular chains and enhanced random entanglement significantly improved the material's mechanical properties, enabling repeated folding without brittle fracture. Fig. 6c demonstrates the shape recovery process of solid–solid phase change membranes: they were first cut into a pentagram shape, then folded and placed near a constant-temperature heat source. Over time, the folded solid–solid phase change membranes gradually regained therr original pentagram form. Fig. 6d further verifies the shape memory functionality of the solid–solid phase change membranes with diverse geometries under temperature stimuli. Solid–solid phase change membranes were fabricated into distinct shapes ("1", "2", "3", "A", "B", "C"), all with a uniform thickness of 0.5 mm. After folding, these samples were exposed to an infrared lamp (simulating a heat source) set at 80 °C – above the solid–solid phase change membranes' phase transition temperature. Within 30 s, the folded solid–solid phase change membranes underwent shape recovery, ultimately reverting from their folded state to their original pre-folded configuration. Fig. 6e presents quantitative data on the shape memory function of the solid–solid phase change membranes. Fig. 6e(I–VIII) shows the entire process of folding and recovery. Under a 60 °C constant-temperature heat source, after folding the solid–solid phase change membrane once, it recovered from 0° to 175° in 155 seconds, achieving a recovery rate of 97.2%. The transition from 20° in Fig. 6(I) to 85° in Fig. 6(V) took 60 s, yielding a one-minute recovery rate of 47.3%. Subsequently, as shown in Fig. 6(VI–VIII), the material progressed from 105° to 175° over 70 s. This result confirms that the geometry of the solid–solid phase change membrane has no significant influence on its thermally induced shape memory capability, thereby expanding its potential applications in information encryption scenarios. Based on the properties of solid–solid phase change membranes, a "shape-encryption-thermally triggered decryption" ABC/123 information encryption demonstration was designed: The membranes are cut into substrates, with specific folds corresponding to the characteristic structures of "ABC" or "123" (*e.g.*, "A" folds into a triangle, "B" into a double arc, and "C" into a semicircle; "1" folds into a vertical line, "2" into a curved line, and "3" into a double arc). The folded shapes are fixed at 25 °C to complete encryption. During transmission, the folded state is conveyed, rendering the information unrecognizable to third parties. For decryption, place the film on a platform heated above 60 °C. The entangled material network dissociates as stress is released, automatically flattening the film. The scrambled characteristics simultaneously revert to clear ABC/123, achieving information decryption. This process leverages the material's low-temperature shape stability and high-temperature self-recovery properties, enabling repeatable demonstrations of information concealment and restoration. The relevant encryption and decryption videos are shown in Fig. S6. After folding and reheating, the entire process can be repeated. After multiple repetitions and being placed in a 90 °C oven, it can still maintain shape stability without liquid leakage, which indicates its potential applications in thermal management.

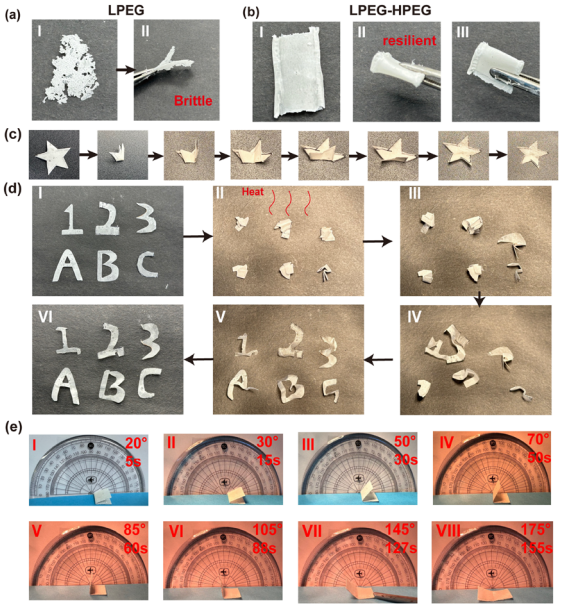

Fig. 6 (a) Photos of pure LPEG phase change membranes with brittle and weak performances. (b) HPEG–LPEG solid–solid phase change membranes with strong and robust performances. (c) Solid–solid phase change membranes were cut into a pentagram shape and folded under simulated sunlight to induce shape recovery, mimicking the shape memory induced by heat. (d) Photos of HPEG–PEG solid–solid phase change membranes in the shapes of "1, 2, 3, A, B, C" placed under simulated heat to induce shape recovery. (e) Quantitative data of HPEG–PEG solid–solid phase change membranes folded and placed under simulated heat to induce shape recovery.

Fig. 7 combines the functions of thermochromic and heat-induced shape memory. Fig. 7a illustrates the mechanism underlying the shape memory and thermochromic behaviours

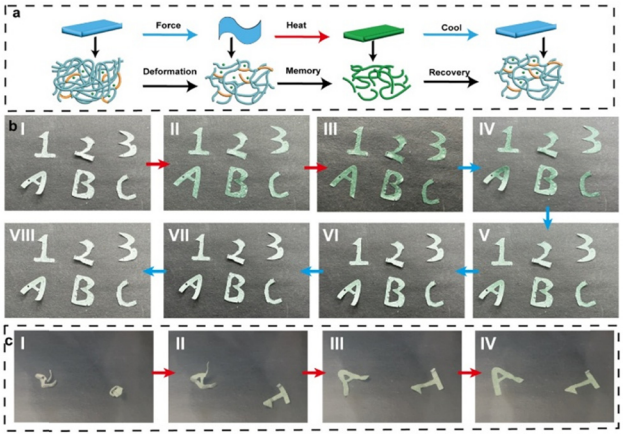

Fig. 7 (a) Schematic illustration of the shape memory and heat induced shape memory mechanism of solid–solid phase change membranes. (b) Solid–solid phase change membranes were cut into specific shapes "1, 2, 3, A, B, C" and placed under a condition of 60 °C to demonstrate the reversible color change. (c) Heat-induced phase change membranes were cut into specific shapes "1, A" and placed under a condition of 80 °C to show reversible color change and heat-induced shape memory.

of solid–solid phase change membranes. The shape memory capability originates primarily from the reversible crystallization–melting transition of HPEG molecular chains, which endows the material with temperature-induced shape memory performance. At ambient temperature, the high crystallinity of HPEG chains within solid–solid phase change membranes form temporary rigid domains; when an external force is applied to deform the material, these rigid domains "lock" the deformed shape. Upon heating above the melting temperature of HPEG, the crystalline regions melt, restoring molecular mobility and releasing the stored elastic energy – this drives the material to revert to its original shape.[50] This shape memory effect depends largely on the reversible crystallization behaviour of HPEG molecular chains, enabling efficient deformation control and repeated cycling within a specific temperature range. For thermochromic behaviour, the microcapsules undergo reversible structural changes: at 60 °C (corresponding to the phase transition temperature of solid–solid phase change membranes), their structure disrupts, causing a colour change from white to green; upon cooling, the structure recovers, and the colour reverts from green to colourless.

To impart thermochromic behaviour, the incorporation of thermochromic nanoparticles enables reversible colour change in solid–solid phase change membranes, while preserving the intrinsic shape memory mechanism of HPEG. Fig. 7b shows the temperature-dependent behaviour of solid–solid phase change membranes doped with thermochromic nanoparticles: as temperature increases, the microcapsules within the nanoparticles rupture, causing the membrane to turn green; upon cooling, the microcapsules undergo reversible recovery, restoring the material to its colourless state.[51] This confirms that introducing thermochromic components achieves temperature-induced reversible colour transformation. Notably, the temperature of this reversible colour change corresponds to the phase transition temperature of PEG – allowing the integration of shape memory and colour change functionalities. Specifically, when the temperature reaches the phase transition temperature, the folded solid–solid phase change membranes not only revert to their original shape but also synchronously change colour to green. Fig. 7c demonstrates the integration of thermochromic properties with thermally induced shape memory. After cutting the solid–solid phase change membranes into specific shapes, they were folded and placed near a simulated heat source set at 80 °C. As the temperature rises, the membranes undergo a colour change while simultaneously restoring their shape, gradually transforming from a white folded state to their original green form. Consequently, these multifunctional solid–solid phase change membranes exhibit significant application potential in smart responsive materials for information encryption and flexible sensor technologies. Video S1 shows the video of thermochromic and thermally induced shape memory properties. Sample B2 was cut into the shapes of "A, 1" and put into an oven set to 80 °C. As the temperature rises, the folded sample B2 rapidly returns to its original shape while turning green, consistent with the mechanism explanation.

Photoluminescence of solid–solid phase change membranes

The photoluminescence mechanism involves LAL particles absorbing external visible light, which excites internal electrons from a stable "low-energy state" to an active "high-energy state" (energy level transition). These unstable high-energy electrons rapidly release energy to reach a metastable "transitional high-energy state", then relax back to the low-energy state, emitting excess energy as photons to complete the photoluminescence process.[52] What's more, the addition of LAL reduces the thermodynamic property of solid–solid phase change membranes. Fig. S7 indicates that the addition of LAL lowers the ΔH_m to 106.9 J g^{-1} and ΔH_c to 107.1 J g^{-1}. The structures of solid–solid phase change membranes with or without LAL particles are shown in Fig. S8(a) and (b). Compared with the phase change membrane without LAL particles, the SEM image clearly reveals the surface morphology of the solid–solid phase change membranes loaded with luminescent LAL material. The image shows that LAL particles exhibit relatively uniform sizes of approximately 0.5–1.0 μm, presenting a regular dot-like structure, indicating excellent particle size control during material preparation. In terms of distribution, LAL particles are uniformly dispersed across most of the flat regions of the HPEG–LPEG matrix. They are embedded as individual particles within the fine surface texture of the film, with no large-area agglomeration observed. This indicates good compatibility between LAL and the solid–solid phase change membranes. However, at the edges of linear cracks in the images, LAL particles exhibit significant local enrichment, forming sawtooth-like protrusions. This aggregation arises from interfacial stresses caused by the difference in thermal expansion coefficients between LAL and the HPEG–LPEG matrix, which

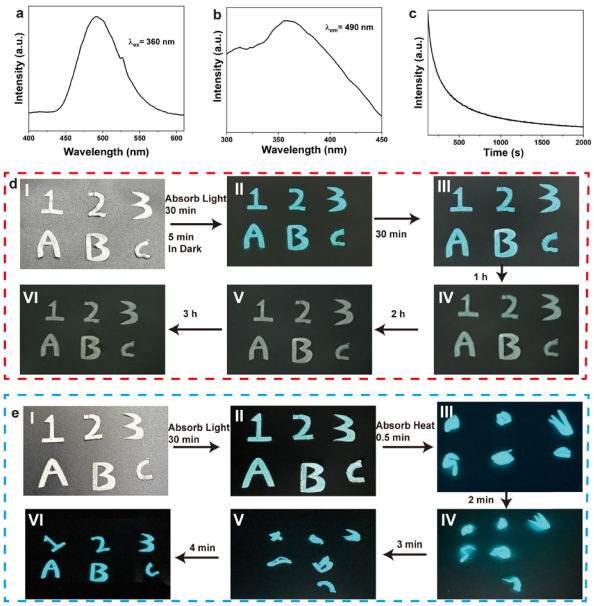

Fig. 8 (a) Photoluminescence emission spectra of LAL–solid–solid phase change membranes (excitation wavelength = 360 nm). (b) Photoluminescence excitation spectra of LAL–solid–solid phase change membranes (emission wavelength = 360 nm). (c) Afterglow decay curve of LAL–solid–solid phase change membranes. (d) Photos of LAL–solid–solid phase change membranes in the dark after (I): light absorption for 30 min, (II): in the dark for 30 min, (III): in the dark for 1 h, (IV): in the dark for 2 h, and (V): in the dark for 2 h. (e) Photoluminescence and heat induced shape memory: after absorbing light and being folded, at a temperature of 90 °C; (I): absorb light for 30 min, (II): absorb heat for 0.5 min, (III): absorb heat for 2 min, (IV): absorb heat for 3 min, and (V): absorb heat for 4 min; the LAL–solid–solid phase change membranes could glow and gradually return to their original shape.

drives particle migration toward defects during crack initiation. Fig. 8 presents the photoluminescent properties of solid–solid phase change membranes. Fig. 8a–c show the photoluminescence spectra of LAL–solid–solid phase change membranes. The LAL–solid–solid phase change membranes show a broad emission band peaking at 490 nm in the wavelength range of 400–625 nm at an excitation wavelength of 360 nm, as shown in Fig. 8a. Excitation by 360 nm ultraviolet light causes Eu^{2+} electrons to transition to a higher energy level. Subsequently, as electrons relax from this higher level back to the lower level, they release photons, producing blue luminescence. The doped Dy^{3+} acts as an auxiliary activator, enhancing the luminescence stability of Eu^{2+} and prolonging the luminescence lifetime through an energy transfer effect. Inspired by the broad emission band peaking at 490 nm in Fig. 8a. Fig. 8b shows the excitation spectrum measured at an emission wavelength of 490 nm. The curve indicates that within the excitation wavelength range of 300–450 nm, the fluorescence intensity first increases and then decreases with increasing excitation wavelength, peaking in the 350–370 nm range. This demonstrates that ultraviolet light in this band exhibits the highest excitation efficiency for the material. This is mainly due to the electronic transition properties of Eu^{2+}. The energy of ultraviolet photons at 350–370 nm closely matches the $4f^7 \rightarrow 4f^65d^1$ transition energy level of Eu^{2+}, enabling efficient driving of electrons from the ground state to a high-energy excited state. When electrons relax from the excited state back to the ground state, they emit blue fluorescence at 490 nm. The doped Dy^{3+} acts as an auxiliary activator, capturing and transferring energy to Eu^{2+} *via* an energy transfer effect. This reduces energy loss from non-radiative transitions, thereby enhancing the luminescence intensity and stability of Eu^{2+}. Fig. 8c shows the afterglow decay curve. The curve exhibits a two-stage decay pattern: during the initial phase (0–500 s), the fluorescence intensity decreases rapidly, while in the subsequent phase (500–2000 s), the decay rate slows significantly. Even at 2000 s, a certain level of luminescence intensity persists, demonstrating the characteristic of long afterglow luminescence. This mainly arises from the synergistic interaction between Eu^{2+} and Dy^{3+}: during excitation, Eu^{2+} absorbs ultraviolet light energy to transition to a higher energy level, while Dy^{3+} acts as a trap center to capture and store a portion of this energy. After excitation ceases, the high-energy electrons of Eu^{2+} rapidly relax back to the ground state, causing a sharp drop in fluorescence intensity during the initial phase. Meanwhile, the energy stored by Dy^{3+} is gradually released to Eu^{2+} through a slow energy transfer process, sustaining its continuous luminescence. Consequently, the decay rate significantly slows down in the later stages. As illustrated in Fig. 8d, LAL were incorporated into the phase change matrix to form LAL–solid–solid phase change membranes. The photoluminescence mechanism proceeds as follows: upon absorbing external visible light, LAL nanoparticles transfer the light energy to internal electrons, triggering their transition from a stable "low-energy state" to an active "high-energy state" – a process defined as an energy level jump. These unstable high-energy electrons rapidly release partial energy, transitioning to a slightly lower yet relatively stable "transitional high-energy state". Subsequently, the electrons return from the "transitional high-energy state" to the low-energy state, emitting excess energy in the form of new photons and thus completing the photoluminescence cycle. To evaluate afterglow performance, the LAL–solid–solid phase change membranes were first exposed to light for 30 min, after which the duration of afterglow emission was monitored. The results showed that the afterglow persisted for up to 2 h, confirming the favorable afterglow properties of the incorporated photoluminescent material. Fig. 8e demonstrates the integration of photoluminescent functionality with thermally induced shape memory. After 30 min of illumination, the folded LAL–solid–solid phase change membranes were placed in an oven set at 90 °C. Driven by the reversible crystallization–melting behavior of HPEG molecular chains, the material simultaneously maintained afterglow emission and achieved shape recovery. As observed, the folded LAL–PEG solid–solid phase change membrane system reverted to its original shape, indicating that the incorporation of LAL did not compromise the intrinsic shape memory mechanism of HPEG. Meanwhile, the FT-IR test results in Fig. S9 indicate that the addition of LAL does not affect interfacial properties. The positions and peak of the main absorption peaks in both curves are similar, suggesting that

neither additive disrupts the main chain of the HPEG–LPEG matrix. Characteristic peaks of core functional groups (*e.g.*, C–H and C–O–C bonds within segments) showed no significant shift, indicating no substantial alteration in the conformation of the matrix molecular chains. Both LAL particles and thermochromic additives exhibit excellent interfacial compatibility with the matrix. Consequently, these multifunctional LAL–solid–solid phase change membranes exhibit promising application potential in high-efficiency nighttime signaling and information encryption materials.

Conclusions

In summary, we developed PEG-based solid–solid phase change membranes with shape memory, thermochromic, and photoluminescent properties *via* a facile method. HPEG incorporation enhanced mechanical strength while enabling solid-state phase transition, with a maximum melting enthalpy of 176.7 J g^{-1} and melting temperature up to 71.6 °C. HPEG's disordered chain entanglement improved thermal insulation (ΔT = 23 °C at 90 °C) and infrared shielding. Its reversible crystallization–melting conferred thermally induced shape memory, with folded samples recovering at 60 °C, suitable for thermal management devices. Thermochromic additives enabled reversible white-to-green color change, synergizing with shape memory for information encryption. Photoluminescent components provided 2 h afterglow post-30 min illumination, which is promising for nighttime signaling and coatings. These findings guide multifunctional HPEG–LPEG solid–solid phase change membrane design for diverse thermal management applications.

Author contributions

Xingyu Tian: conceptualization, data curation, investigation, visualization, methodology, writing – original draft; Yinbo Zhao: conceptualization, resources, project administration; Weizhong Yuan: conceptualization, resources, supervision, funding acquisition, project administration, writing – review & editing.

Conflicts of interest

There are no conflicts to declare.

Data availability

Data will be made available on request.

Supplementary information (SI): POM images, DSC curve, TGA curves, stress–strain curves and video of thermochromic and thermal induced shape memory properties. See DOI: https://doi.org/10.1039/d5nj05009j.

Acknowledgements

The project was funded by the National Natural Science Foundation of China (no. 82172040), the National Natural Science Foundation of China (no. 12402171), the Shanghai Pujiang Program (23PJ1414000), and the Fundamental Research Funds for the Central Universities (22120240573). The authors are also thankful for the support from the Experimental Centre of Materials Science and Engineering at Tongji University.

Notes and references

1 G. Simonsen, R. Ravotti, P. O'Neill and A. Stamatiou, *Renewable Sustainable Energy Rev.*, 2023, **184**, 113546.
2 Y. Guo, B. Zhao, H. Guo, Y. Ge, N. Sheng, E. Gariboldi and C. Zhu, *Chem. Eng. J.*, 2024, **487**, 150390.
3 Y.-C. Zhou, J. Yang, L. Bai, R.-Y. Bao, M.-B. Yang and W. Yang, *Chem. Eng. J.*, 2022, **446**, 137463.
4 Y. Yang, X. Cai and W. Kong, *Appl. Energy*, 2023, **332**, 120564.
5 S. An, B. Shi, M. Jiang, B. Fu, C. Song, P. Tao, W. Shang and T. Deng, *Chem. Rev.*, 2023, **123**, 7081–7118.
6 Y. Liao, L. Zhang, X. Xu, W. Yang, F. He, Z. Jiang, N. Chen, Y. Zhou and Y. Li, *ACS Appl. Polym. Mater.*, 2025, **7**, 4584–4595.
7 G. Wang, Z. Tang, Y. Gao, P. Liu, Y. Li, A. Li and X. Chen, *Chem. Rev.*, 2023, **123**, 6953–7024.
8 J. Cui, W. Li, Y. Wang, H. Yu, X. Feng, Z. Lou, W. Shan and Y. Xiong, *Adv. Funct. Mater.*, 2022, **32**, 2108000.
9 S. Wang, X. Jia, B. Liu, X. Li, M. Xu, J. Zhou, Y. Yu and X. Huai, *ACS Appl. Polym. Mater.*, 2023, **5**, 8579–8588.
10 H. Hu, *Composites, Part B*, 2020, **195**, 108094.
11 H. Baniasadi, Z. Fathi, R. Abidnejad, P. E. S. Silva, S. Bordoloi, J. Vapaavuori, J. Niskanen, E. Lizundia, E. Kontturi and J. Lipponen, *Carbohydr. Polym.*, 2025, **367**, 123999.
12 K. Song, F. Liu, J. Song, W. Zhou, Z. Jiang, F. He, G. He, Z. Yang and W. Yang, *ACS Appl. Polym. Mater.*, 2024, **6**, 15105–15113.
13 L. Wang, X. Fu, J. He, X. Shi, T. Chen, P. Chen, B. Wang and H. Peng, *Adv. Mater.*, 2020, **32**, 1901971.
14 A. Usman, F. Xiong, W. Aftab, M. Qin and R. Zou, *Adv. Mater.*, 2022, **34**, 2202457.
15 H. Zhang, Z. Liu, J. Mai, N. Wang, J. Zhong, X. Mai and N. Zhang, *Chem. Eng. J.*, 2021, **411**, 128482.
16 C. Wang, X. Geng, J. Chen, H. Wang, Z. Wei, B. Huang, W. Liu, X. Wu, L. Hu, G. Su, J. Lei, Z. Liu and X. He, *Adv. Mater.*, 2024, **36**, 2309723.
17 Y. Zhao, T. Liu, Z. Wei, A. Yuan, Y. Chen, L. Jiang, J. Lei and X. Fu, *Chem. Eng. J.*, 2023, **462**, 142164.
18 Y. Fang, X. Xiong, L. Yang, W. Yang, H. Wang, Q. Wu, Q. Liu and J. Cui, *Adv. Funct. Mater.*, 2023, **33**, 2301505.
19 M. M. Umair, Y. Zhang, K. Iqbal, S. Zhang and B. Tang, *Appl. Energy*, 2019, **235**, 846–873.
20 L.-S. Tang, J. Yang, R.-Y. Bao, Z.-Y. Liu, B.-H. Xie, M.-B. Yang and W. Yang, *Energy Convers. Manage.*, 2017, **146**, 253–264.
21 Y.-J. He, Y.-W. Shao, Y.-Y. Xiao, J.-H. Yang, X.-D. Qi and Y. Wang, *ACS Appl. Polym. Mater.*, 2022, **14**, 6057–6070.

22 Z. Bai, H. Zhang, H. Zhu, J. Jiang, D. Zhang, Y. Yu and F. Quan, *Carbohydr. Polym.*, 2023, **317**, 121037.
23 K. Yan, Y. Feng and L. Qiu, *Sol. Energy*, 2024, **272**, 112477.
24 M. M. Umair, Y. Zhang, S. Zhang, X. Jin and B. Tang, *J. Mater. Chem. A*, 2019, **7**, 26385–26392.
25 K. Balasubramanian, A. Kumar Pandey, R. Abolhassani, H.-G. Rubahn, S. Rahman and Y. Kumar Mishra, *Chem. Eng. J.*, 2023, **462**, 141984.
26 J. Shi, W. Aftab, Z. Liang, K. Yuan, M. Maqbool, H. Jiang, F. Xiong, M. Qin, S. Gao and R. Zou, *J. Mater. Chem. A*, 2020, **8**, 20133–20140.
27 S. Sundararajan, A. B. Samui and P. S. Kulkarni, *J. Mater. Chem. A*, 2017, **5**, 18379–18396.
28 Z. Wang, S. Liu, C. Zhu and J. Xu, *Adv. Mater.*, 2024, **36**, 2403889.
29 M. M. Crowley, F. Zhang, J. J. Koleng and J. W. McGinity, *Biomater*, 2002, **23**, 4241–4248.
30 W. Su, J. Darkwa and G. Kokogiannakis, *Renewable Sustainable Energy Rev.*, 2015, **48**, 373–391.
31 Y. Wu, M. Chen, G. Zhao, D. Qi, X. Zhang, Y. Li, Y. Huang and W. Yang, *Adv. Mater.*, 2024, **36**, 2311717.
32 E. van Ruymbeke, Y. Masubuchi and H. Watanabe, *Macromolecules*, 2012, **45**, 2085–2098.
33 T. Shahid, Q. Huang, F. Oosterlinck, C. Clasen and E. van Ruymbeke, *Soft Matter*, 2017, **13**, 269–282.
34 M. Gordon, *Polymers*, 1981, **22**, 565.
35 Z. Wang, M. Schaller, A. Petzold, K. Saalwächter and T. Thurn-Albrecht, *Macromolecules*, 2024, **57**, 1632–1641.
36 S. S. A. Shuaib, Z. Niu, Z. Qian, S. Qi and W. Yuan, *Cellulose*, 2023, **30**, 1841–1855.
37 K. Zhang, X. Zhou, S. Li, L. Zhao, W. Hu, A. Cai, Y. Zeng, Q. Wang, M. Wu, G. Li, J. Liu, H. Ji, Y. Qin and L. Wu, *Adv. Mater.*, 2023, **35**, 2305472.
38 K. Saalwächter, T. Thurn-Albrecht and W. Paul, *Macromol. Chem. Phys.*, 2023, **224**, 2200424.
39 M. Rubinstein and S. Panyukov, *Macromolecules*, 2002, **35**, 6670–6686.
40 M. E. De Rosa and H. H. Winter, *Rheol. Acta*, 1994, **33**, 220–237.
41 C. Norioka, Y. Inamoto, C. Hajime, A. Kawamura and T. Miyata, *NPG Asia Mater.*, 2021, **13**, 34.
42 S. S. Hou and P. L. Kuo, *Polymers*, 2001, **42**, 2387–2394.
43 K. Pielichowski and K. Flejtuch, *Polym. Adv. Technol.*, 2002, **13**, 690–696.
44 W. Aftab, X. Huang, W. Wu, Z. Liang, A. Mahmood and R. Zou, *Energy Environ. Sci.*, 2018, **11**, 1392–1424.
45 Y. Du and Y. Dai, *Energy*, 2018, **161**, 233–250.
46 A. A. Rodríguez Soto, J. L. Valín Rivera, L. M. Sanabio Alves Borges and J. E. Palomares Ruiz, *Polymers*, 2022, **14**, 4634.
47 J. Qin and S. T. Milner, *Macromolecules*, 2014, **47**, 6077–6085.
48 K. Kremer and G. S. Grest, *Energy Environ. Sci.*, 1990, **92**, 5057–5086.
49 S. Yousefi and M. Saraji, *Spectrochim. Acta, Part A*, 2019, **213**, 1–5.
50 J. Sringam, T. Kajornprai, T. Trongsatitkul and N. Suppakarn, *Polymers*, 2025, **17**, 225.
51 Y. Zhou and R. Duan, *ACS Appl. Energy Mater.*, 2024, **7**, 5944–5956.
52 Y. Li, M. Gecevicius and J. Qiu, *Chem. Soc. Rev.*, 2016, **45**, 2090–2136.

